



Ultrafast activation of Ni foam by electro-corrosion and its use for upcycling PBT plastic waste

Xuan Liu^a, Jianying Wang^a, Zhongying Fang^b, Shuaiqi Gong^a, Dengke Xiong^a, Wei Chen^b,
Deli Wu^c, Zuofeng Chen^{a,*}

^a Shanghai Key Lab of Chemical Assessment and Sustainability, School of Chemical Science and Engineering, Tongji University, 1239 Siping Road, Shanghai 200092, China

^b State Key Laboratory of Electroanalytical Chemistry, Changchun Institute of Applied Chemistry, Chinese Academy of Sciences, Changchun 130022, China

^c State Key Laboratory of Pollution Control and Resources Reuse, College of Environmental Science & Engineering, Tongji University, Shanghai 200092, China

ARTICLE INFO

Keywords:

Polybutylene terephthalate (PBT) upcycling
Electro-corrosion engineering
1,4-Butanediol oxidation
Succinate
Ni foam electrode

ABSTRACT

Herein, an ultrafast electro-corrosion approach is developed for activating Ni foam (NF) into an efficient electrocatalyst for upcycling polybutylene terephthalate (PBT) waste plastic. The electro-corrosion process assisted by Cl^- is completed by only 6 CV cycles (~ 3 min) and the activity of the treated NF (T-NF), characterized by the integrated $\text{Ni}^{2+}/\text{Ni}^{3+}$ peak area is enhanced by 150 times. The T-NF electrode exhibits excellent catalytic activity toward 1,4-butanediol oxidation, delivering a current density of 50 mA cm^{-2} at 1.36 V (vs. RHE). This allows the electrocatalytic reforming of 1,4-butanediol component in PBT hydrolysate into succinate with a high Faraday efficiency 93%. The in-situ Raman and FTIR spectroscopies combining density functional theory calculations identify catalytically active centers, critical intermediates, and favorable pathway for 1,4-butanediol oxidation to succinate. This work provides an ultrafast one-step surface engineering strategy to turn pristine Ni foams into high-performance electrocatalysts for upcycling PBT plastic and other electrochemical applications.

1. Introduction

The widely employed approaches for preparing electrocatalysts, such as high-temperature calcination, hydrothermal or solvothermal methods, usually involve complex synthesis steps, harsh reaction conditions, or large energy consumption [1–4]. In particular, the practical application of electrocatalysts requires large-scale production with high reproducibility, which imposes stricter restrictions on the preparation of electrocatalysts [5–8]. Therefore, the development of facile and general strategies for synthesizing efficient and robust transition metal-based electrocatalysts with well controllability is essential for future industrialized applications [9–12].

Corrosion engineering is an effective method for preparing catalysts by manipulating the corrosion reaction on the metal surface [13]. The pristine metal substrates usually possess poor electrocatalytic activities with dense passivation layers. These substrates can be corroded and thus modified by strong corrosive agents such as O_2 , Fe^{3+} , and Cl^- . In particular, Cl^- is well known as a corrosion accelerant for its strong penetration, coordination and depassivation abilities [14]. After the

corrosion reaction, the active layers may be formed on the surface of the metal substrates, serving as the catalytic species [15]. There have been many studies employing chemical corrosion to fabricate advanced electrocatalysts based on metal powders and metal foams of nickel, iron, and alloys [16–20]. However, the electro-corrosion strategy that combines virtues of both chemical corrosion and electrochemistry has been seldom reported to fabricate catalytic electrodes. Through the electro-corrosion strategy, the widely used Ni foam electrode can be readily promoted to be used for industrialized electrolyzers [21–23].

Polybutylene terephthalate (PBT) is an engineering thermoplastic with excellent properties formed by polymerization of terephthalic acid (TPA) and 1,4-butanediol (BDO) monomers [24]. For widespread use, PBT waste plastic will bring serious environmental pollution and resource waste [25,26]. Fortunately, the polyester nature of PBT makes it hydrolyzable into corresponding monomers, which can be further transformed into valuable products. Upgrading PBT waste plastic into value-added succinate through electrocatalytic reforming following chemical hydrolysis is sustainable and economically profitable. Succinate, as one of the important platform chemicals is widely used in food,

* Corresponding author.

E-mail address: zfchen@tongji.edu.cn (Z. Chen).

<https://doi.org/10.1016/j.apcatb.2023.122870>

Received 14 March 2023; Received in revised form 5 May 2023; Accepted 8 May 2023

Available online 9 May 2023

0926-3373/© 2023 Elsevier B.V. All rights reserved.

medicine, and chemical industry fields [27–29]. It is estimated that the global succinic acid and succinate market will steadily grow at a compound annual growth rate of around 27.4% to reach \$1.8 billion (768 million tonnes at \$2.3/kg) in 2025 [27]. Although studies on electrocatalytic reforming of PET waste plastic have been reported, there are no related studies dealing with PBT waste plastic [30–36].

Herein, we developed an ultrafast and versatile electro-corrosion strategy for in-situ transformation of Ni foam into a high-performance, self-supporting electrocatalyst for upcycling PBT. In saturated NaCl solution, Ni foam can be effectively activated by only 6 CV scan cycles

(around 3 min) under room temperature. The performance of the treated NF (T-NF) electrode can be readily regulated by changing the CV scan pattern and exhibits greatly enhanced catalytic activity by 150 times. It delivers a current density of 50 mA cm^{-2} at a low potential of 1.36 V (vs. RHE) for the 1,4-butanediol oxidation reaction (BOR) with a high Faraday efficiency of 93% for succinate production. The in-situ Raman and FTIR spectroscopies and DFT calculations reveal the reaction mechanism and optimal reaction pathway of BOR over the T-NF electrode.

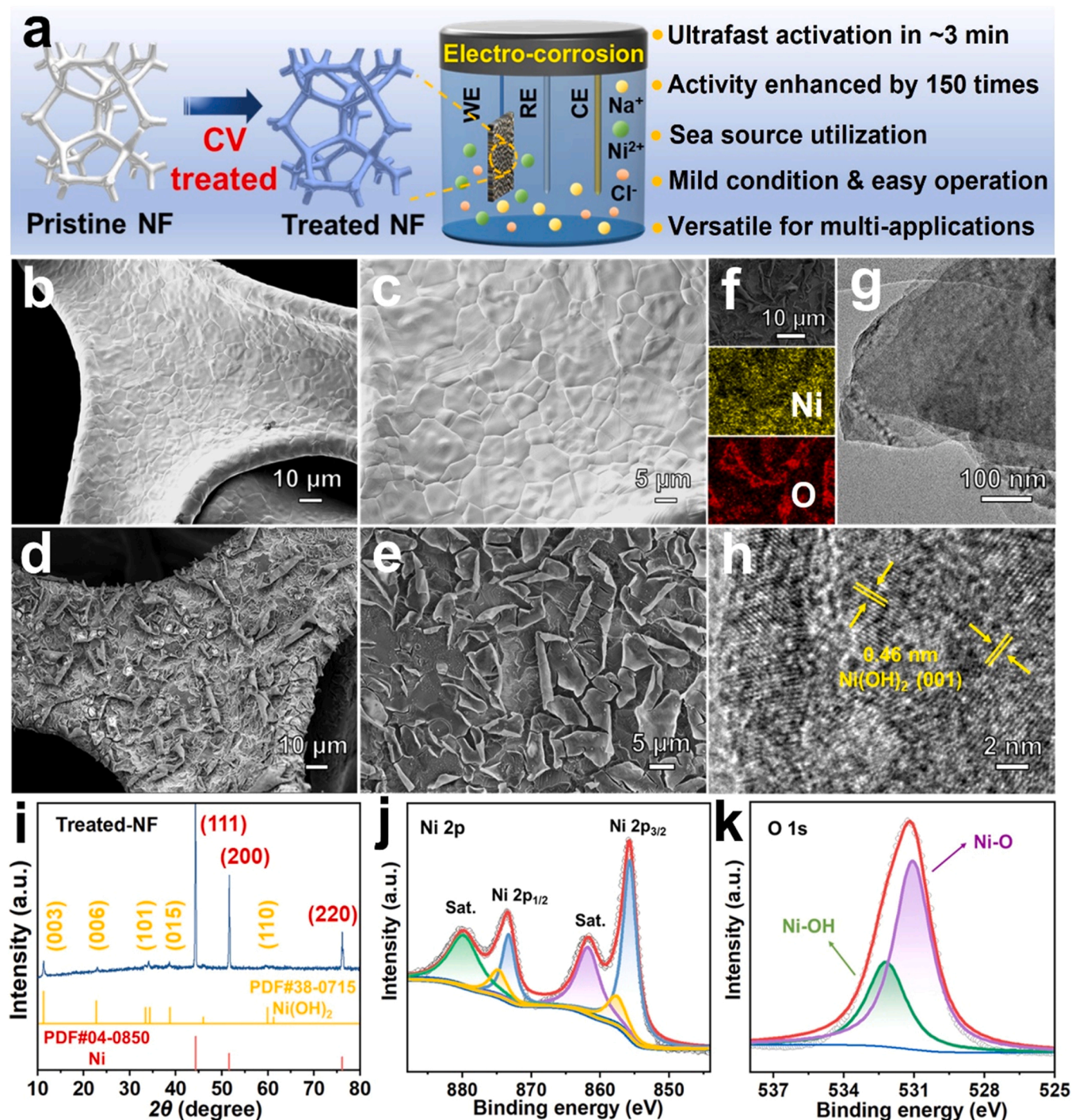


Fig. 1. (a) Schematic illustration for preparing the T-NF through the electro-corrosion method. (b, c) SEM images of P-NF and (d, e) the T-NF. (f) Elemental mapping images of Ni and O elements in the T-NF. (g) TEM and (h) HRTEM images of the T-NF. (i) XRD pattern of the T-NF. High-resolution XPS spectra for (j) Ni 2p and (k) O 1s.

2. Experimental section

2.1. Chemicals

Sodium chloride (NaCl, 99%) and potassium hydroxide (KOH, 99%) were purchased from Sinopharm Chemical Reagent Co. Ltd. 1,4-butanediol (99%), terephthalic acid (TPA, 99%), succinate (99.5%), maleic acid (99%) and deuterated water (D₂O) were purchased from Macklin Biochemical Co., Ltd. Polybutylene terephthalate (PBT) powder (150 mesh, 99%) were purchased from Shanghai Aladdin Regent Co., Ltd. All other chemical reagents were of analytical grade and used as received without further purification. All electrolyte solutions were prepared by Milli-Q ultrapure water (18 MΩ cm).

2.2. Preparation of the T-NF via the electro-corrosion strategy

In a three-electrode configuration, saturated NaCl solution was used as electrolyte, and graphite rod and Hg/HgO were used as the counter and reference electrodes, respectively. The pristine nickel foam was scanned between −0.7 and 1.0 V (vs. RHE) at a scan rate of 100 mV/s for several cycles. Finally, the treated nickel foam was washed with deionized water for several times, and then dried at 60 °C under vacuum.

2.3. Product analysis

To determine the products of BDO oxidation and calculate Faradaic efficiencies, the long-term bulk electrolysis was carried out in a three-electrode system at the constant potential of 1.45 V (vs. RHE) in 1.0 M KOH with 0.1 M 1,4-butanediol under vigorous stirring at room temperature. The electrolyte solutions were collected after approximately 12 h electrolysis and then analyzed by the nuclear magnetic resonance (NMR) spectroscopy. During the measurement, 500 μL electrolyte was added into 100 μL D₂O, and maleic acid was used as an internal standard. The Faradaic efficiencies (FE) for the production of succinate were calculated by the following equation: $FE = (n \times z \times F/Q) \times 100\%$, where n is the yield of succinate (mol), z is the number of electrons required to form a molecule of succinate, Q is the quantity of electric charge (C), and F is the Faraday constant (96,485 C mol^{−1}).

3. Results and discussion

3.1. Material characterization

As illustrated in Fig. 1a, the T-NF is prepared via an ultrafast one-step electro-corrosion approach assisted by NaCl. Briefly, in a three-electrode system configuration, a piece of pristine Ni foam (P-NF) serving as the working electrode was subjected to cyclic voltammetric (CV) scan in saturated NaCl electrolyte solution at room temperature. After 6 scan cycles (around 3 min), the self-supporting T-NF was collected and directly used as the catalytic electrode for the BOR and PBT upcycling. A detailed synthetic procedure is described in the Experimental section in the Supporting Information.

The morphologies of the P-NF and T-NF were characterized by scanning electron microscopy (SEM) and transmission electron microscopy (TEM). As shown in Fig. 1b, the Ni foam has the three-dimensional (3D) skeleton structure. The high-magnification SEM image in Fig. 1c shows that the P-NF possesses a smooth surface without any cracking. After the electro-corrosion treatment in saturated NaCl solution, the T-NF still maintains the 3D skeleton structure, as shown in Fig. 1d. Compared with the P-NF, the high-magnification SEM image in Fig. 1e shows that the T-NF becomes quite rough, and abundant nanosheets are uniformly grown throughout the surface of NF substrates, which increases active sites and accelerates mass transport to promote the electrocatalytic activity. The energy dispersive X-ray spectroscopy (EDS) elemental mapping images of the T-NF show the uniform dispersion of

Ni and O elements, as shown in Fig. 1f. The TEM image of the material scraped from the NF surface in Fig. 1g presents the nanosheet morphology. The high-resolution TEM (HRTEM) image in Fig. 1h displays a lattice spacing of 0.46 nm, corresponding to the (001) plane of Ni(OH)₂.

The X-ray diffraction (XRD) pattern of the T-NF in Fig. 1i shows three sharp peaks at 44.5°, 51.8°, and 76.4°, belonging to the (111), (200) and (220) planes of Ni foam (PDF # 04-0850). By electro-corrosion treatment, a set of weak diffraction peaks appear at 11.3°, 22.8°, 34.3°, 38.8° and 59.7°, attributed to (003), (006), (101), (015) and (110) planes of Ni(OH)₂ (PDF # 38-0715). It indicates that the grown corroded layers are mainly nickel hydroxides. The survey X-ray photoelectron spectroscopy (XPS) in Fig. S1 reveals the existence of Ni and O on the T-NF surface. Fig. 1j shows a high-resolution Ni 2p XPS. By deconvolution, the two main peaks located at 855.7 and 873.5 eV can be assigned to Ni²⁺ 2p with two shoulder peaks at 857.8 and 875.1 eV for Ni³⁺ 2p. The peaks at 861.8 eV and 880.1 eV are identified as the satellite peaks of Ni 2p_{3/2} and Ni 2p_{1/2}, respectively [18]. The O 1s XPS in Fig. 1k can be divided into two contributors. The peak at 531.1 eV is typical of metal-oxygen bonds (Ni-O), while the peak at 532.2 eV can be assigned to the Ni-OH bond [37]. The results of these characterizations reveal the formation of surficial nickel oxide or hydroxide by the electro-corrosion treatment.

3.2. Growth process and mechanism

The catalytic electrodes were prepared through an ultrafast one-step electro-corrosion method by simple CV scans. As shown in Fig. 2a, the first pattern of CV scan has a voltage window of 0–1.0 V (vs. RHE), denoted as CV-1. The anodic current response in the potential from 0.5 to 1.0 V is associated with Ni corrosion to generate Ni cation. The current is increased with the increase of CV scan cycles, indicating that the etching process occurs effectively on the surface of the Ni foam. Fig. 2b shows the second CV scan pattern with a voltage window of −0.7–1.0 V (vs. RHE), denoted as CV-2. The reduction current in the potential from −0.7 to −0.30 V is associated with the electrochemical re-deposition of Ni cation produced from the anodic dissolution. It is noted that the anodic corrosive current between 0.5 and 1.0 V is slightly decreased after scanning for > 6 cycles. It indicates that the continuous oxidative etching is passivated by the re-deposited layer from the cathodic scan. Fig. 2c shows the optical photos of P-NF and T-NF via different CV scan patterns. The T-NF by CV-1 exhibits obvious destruction at the edge, revealing the strong corrosive effect on the NF by continuous oxidative scan. In contrast, the T-NF by CV-2 retains good integrity but loses its metallic luster. It suggests again that the re-deposition of Ni cation in the cathodic scan protects the NF from continuous corrosion and ensures the uniform growth of the corrosion layer.

The effect of CV scan cycles on the surface morphology of the T-NF was further investigated. As shown in Fig. 2d, CV-1 treatment results in no obvious change on the surface of Ni foam even after 10 scan cycles. For comparison, CV-2 treatment induces significant roughening effect on the morphology which is pronounced with increasing CV scan cycles, Fig. 2e–g. Noticeably, the surface with nanosheets is destroyed after 8 scan cycles in CV-2 treatment, suggesting the exorbitant corrosion. After CV-2 treatment, the concentration of Ni cation in the electrolyte was determined by inductively coupled plasma - optical emission spectrometer (ICP-OES) (Fig. S2). The initial concentration of Ni cation increases rapidly and then gradually slows down upon increasing the scan cycles. The result is associated with the cathodic re-deposition following the anodic dissolution.

To verify the important role of Cl[−] in the corrosion process, we performed electro-corrosion treatment on Ni foam in NaNO₃, Na₂SO₄, NaClO₄, and Na₂S solutions (Figs. S3–S6). Compared with the treatment carried out in NaCl solution, there are no obvious anodic currents observed in NaNO₃, Na₂SO₄, NaClO₄, and Na₂S solutions, indicating negligible electro-corrosion effect. Accordingly, the morphologies of

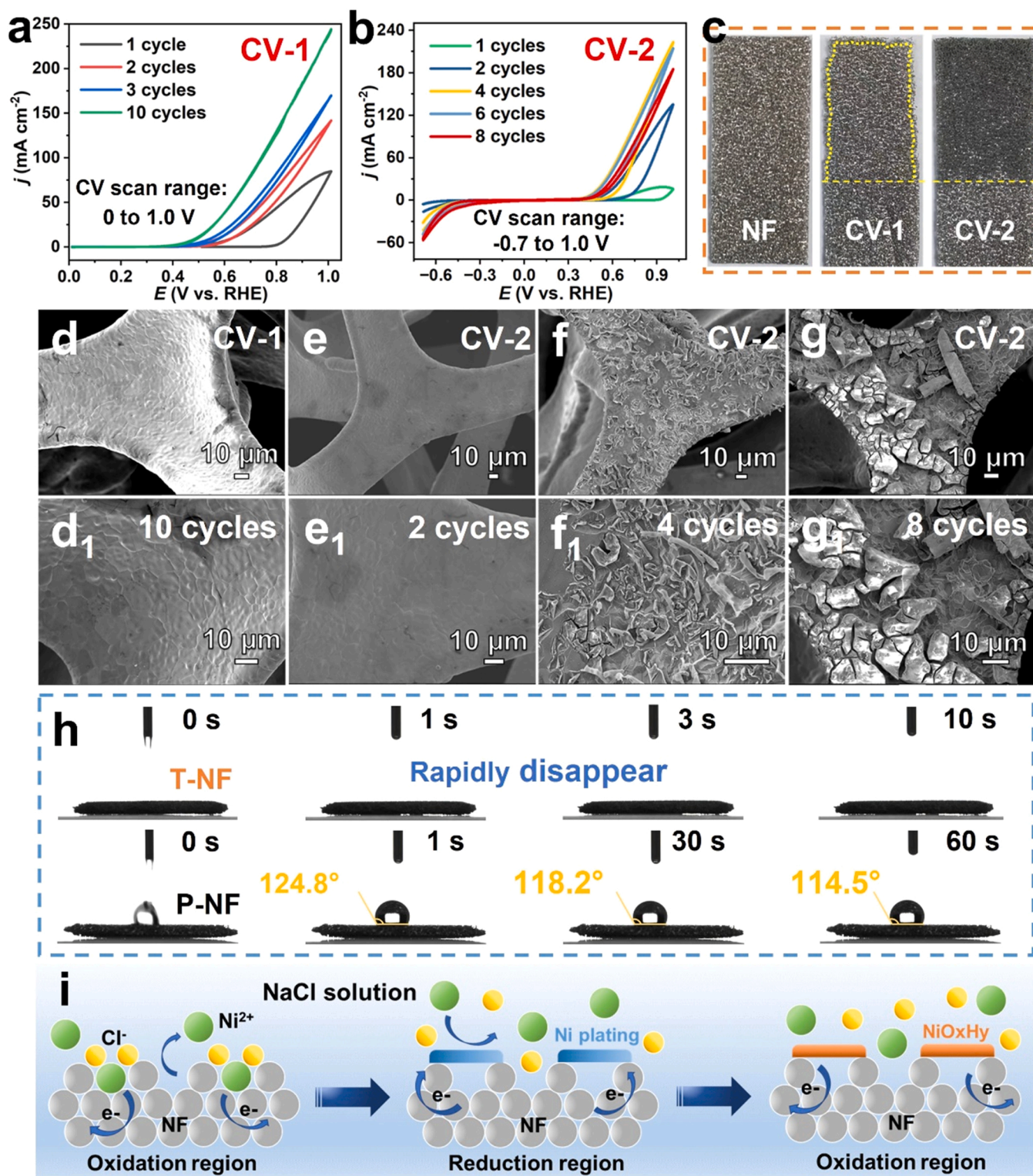


Fig. 2. (a, b) CV curves for preparing electrodes. (c) Photographs of P-NF and T-NF. (d-g) SEM images of the as-prepared materials via different CV scan patterns. (h) Photos of contact angles of P-NF and T-NF. (i) Simulated diagram of the electro-corrosion mechanism in NaCl solution.

NFs are not modified after CV scans in these solutions. It is noted that the use of chloride ions as corrosion accelerant can take the advantage of sea source. Chloride ions abundant in seawater play a “destructive” role in metal passivation or protection but a “constructive” role for the electrode preparation in this study.

The favorable wetting is an important factor for the electrocatalytic performance, which enables the catalytically active sites more accessible

[38–40]. As shown in Fig. 2h, the liquid drop of 1.0 M KOH solution can remain for 60 s on the surface of the P-NF, while the liquid drop disappears quickly on the T-NF, confirming the better wetting of the T-NF due to its hydrophilic nature.

Based on the above analysis, the electro-corrosion grown mechanism of T-NF in NaCl solution is schematically illustrated in Fig. 2i. First, the NF was anodically corroded to generate Ni²⁺ ions with the assistance of

Cl^- anions (from 0.5 V to 1.0 V). By reversing the CV scan with the potential reaching Ni^{2+} reduction (from -0.3 to -0.7 V), the electrochemical re-deposition of nickel occurs. In the subsequent cycles, the newly deposited Ni is oxidized to produce nanosized NiO_xH_y on the surface of NF, which passivates the continuous corrosion and ensures the uniform growth of the corrosion layer.

3.3. Electrocatalytic performance toward BDO oxidation and PBT upcycling

The electrocatalytic performance toward the BOR was evaluated in a three-electrode configuration with the T-NF electrode. Fig. 3a presents the linear sweep voltammetric (LSV) curves of the P-NF and T-NF in 1.0 M KOH with and without 0.1 M 1,4-butanediol (BDO). The T-NF shows high OER activity in 1.0 M KOH reaching a current density of 50 mA cm^{-2} at 1.57 V, and this value significantly decreases to 1.36 V after adding 0.1 M BDO. For comparison, the P-NF exhibits poor OER

and BOR activities. Fig. 3b shows that the T-NF has a smaller slope for the BOR (63.4 mV dec^{-1}) than for OER ($228.9 \text{ mV dec}^{-1}$), implying a more favorable catalytic kinetics. Electrochemical impedance spectroscopy (EIS) was performed to investigate the BOR kinetics. As shown in Fig. 3c, the T-NF achieves a much lower charge transfer resistance (R_{ct}) compared with the P-NF. In Fig. S7, the charge transfer resistance is decreased as the overpotential is increased, which is also consistent with the rapid BOR kinetics at the T-NF. In the contrast experiments, the NFs treated with NaNO_3 , Na_2SO_4 , NaClO_4 , or Na_2S as electrolyte by a similar procedure exhibit insignificant catalytic activities toward the BOR, as shown in Fig. S8. The results further suggest the important role of Cl^- in facilitating the electro-corrosion process and promoting the catalytic performance.

The OER and BOR performances of the T-NF prepared by different CV scan cycles in saturated NaCl solution were also investigated. As shown in Fig. 3d, with the increase of scan cycles, the oxidation peak of $\text{Ni}^{2+}/\text{Ni}^{3+}$ becomes much more pronounced, indicating the effective

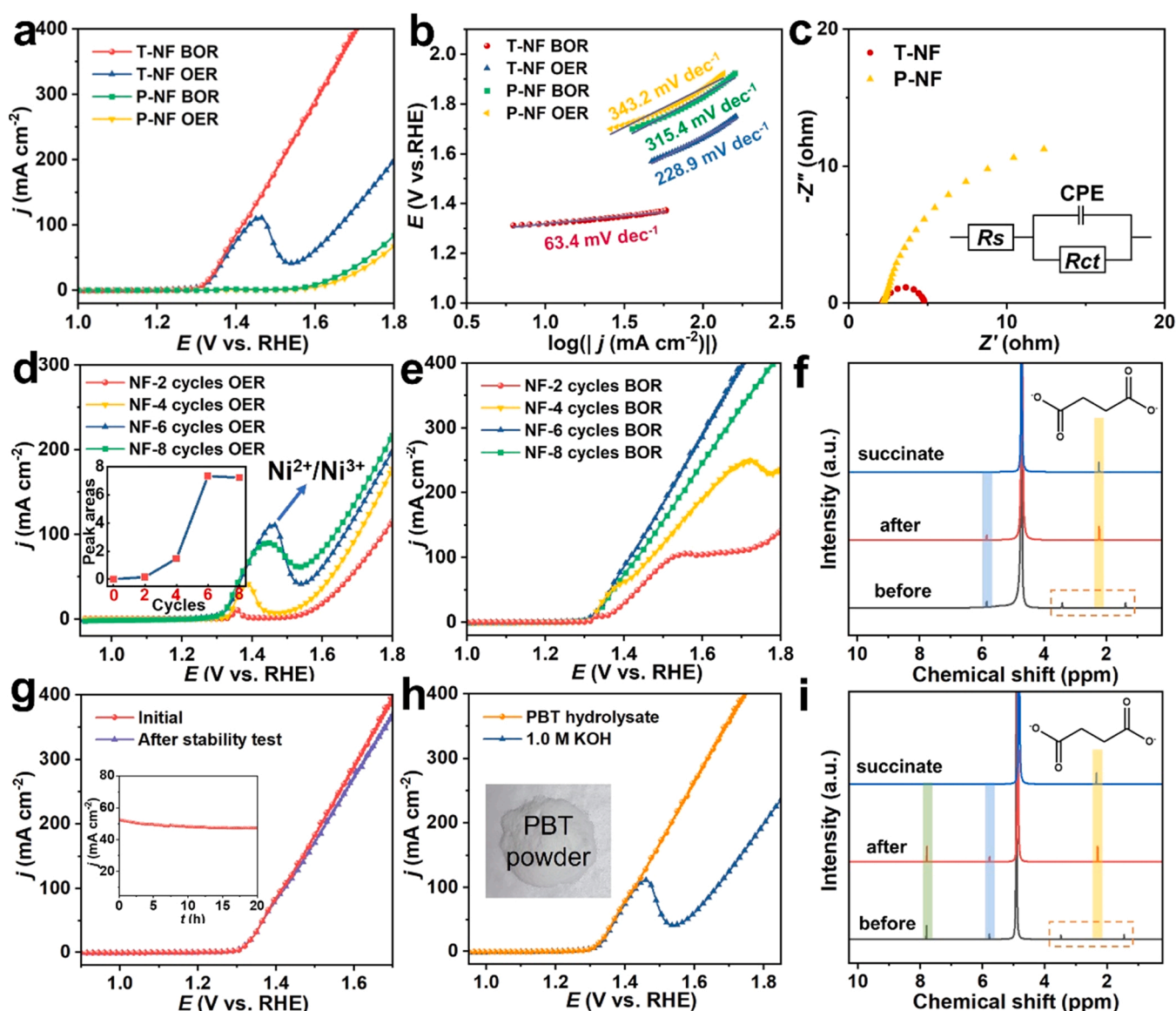


Fig. 3. (a) LSV curves and (b) Tafel plots for the T-NF in 1.0 M KOH with and without 0.1 M BDO; (c) Nyquist plots of the P-NF and T-NF for BDO oxidation; (d) OER LSV curves and the integrated $\text{Ni}^{2+}/\text{Ni}^{3+}$ peak areas (the inset) of the T-NF treated with different CV scan cycles; (e) BOR LSV curves of the T-NF treated with different CV scan cycles; (f) ¹H NMR spectra for products of BDO oxidation; blue-internal standard, yellow-succinate, and red dashed-BDO. (g) The long-term electrolysis of the T-NF in 1.0 M KOH containing 0.1 M BDO; LSV curves for the T-NF before and after the stability test. (h) LSV curves for the T-NF in 1.0 M KOH and PBT hydrolysate. (i) ¹H NMR spectra for products of the PBT hydrolysate oxidation; green-terephthalate.

activation of the surface of NF. The inset in Fig. 3d shows that the integrated $\text{Ni}^{2+}/\text{Ni}^{3+}$ peak area reaches its maximum at 6 scan cycles, which is around 150 times higher than that of the P-NF. Accordingly, the T-NF by 6 scan cycles exhibits the highest BOR activity, as shown in Fig. 3e. Together, these results demonstrate that the BOR performance of the T-NF can be effectively tailored by NaCl-assisting electro-corrosion through simple CV scanning.

The oxidation product of 1,4-butanediol after long-term electrolysis was measured by ^1H nuclear magnetic resonance (NMR) spectroscopy. The amounts of succinate product were calculated by the standard curve method in Fig. S9. The Faradaic efficiency (FE) of the T-NF for the conversion of BDO to succinate can reach over 93% at the optimum potential of 1.45 V (vs. RHE) (Fig. S10). After the complete electrolysis at 1.45 V, the ^1H NMR spectra in Fig. 3f show that the signals of BDO at 3.41 ppm and 1.39 ppm disappear with a strong peak of succinate appearing at 2.22 ppm, indicating the efficient conversion of BDO to succinate. To estimate the durability of the T-NF, a long-term electrolysis test was performed in 1.0 M KOH containing 0.1 M BDO. As shown in Fig. 3g, the electrolysis current is only slightly decreased presumably due to the consumption of the reagent and the variation of the LSV curve is insignificant after the electrolysis test. The SEM image in Fig. S11 shows that the nanosheet morphology of the T-NF is well preserved after the long-term durability test. The HRTEM image in Fig. S12 shows lattice fringes with interplanar distances of 0.240 nm for (002) plane of NiOOH, consistent with the formation of NiOOH on the surface of T-NF after BOR. The Ni 2p XPS after BDO oxidation in Fig. S13 displays two peaks at 875.1 and 857.2 eV for Ni^{3+} 2p_{3/2} and 2p_{1/2}, respectively, consistent with formation of NiOOH species on the surface of NF.

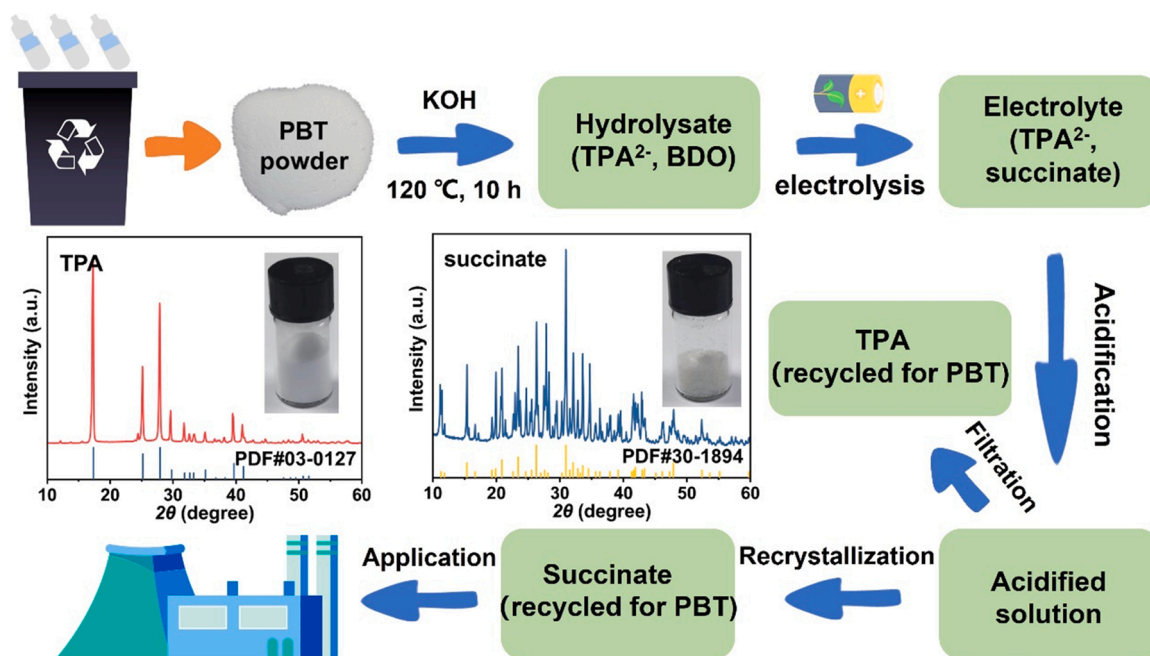
Unrecycled PBT waste can cause serious environmental problems. In an alkaline solution, PBT can be hydrolyzed into its monomers including BDO and TPA, noting the details in the Supporting Information. The amount of BDO obtained from hydrolysis of PBT powder was calculated via the standard curve method in Fig. S14. The PBT hydrolysate was then employed as the electrolyte solution for the electrocatalytic measurements. Fig. 3h shows LSV curve of the T-NF in the PBT hydrolysate solution, which follows the BOR catalytic behavior. The oxidation product of PBT hydrolysate was analyzed by ^1H NMR in Fig. 3i. For PBT hydrolysate, peaks in the spectrum are identified as TPA^{2-} (7.68 ppm)

and 1,4-butanediol (3.41 and 1.39 ppm). Electrolysis at 1.45 V results in the disappearance of 1,4-butanediol and the appearance of succinate at 2.22 ppm with the signal for TPA^{2-} unaltered. As a result, 1,4-butanediol in the PBT hydrolysate is transformed into value-added succinate.

To extend the economic potential of the electrocatalytic upcycling of PBT waste, we separated and purified the PBT hydrolysate after electrolysis. As shown in Scheme 1, TPA can be easily precipitated through acidification of the electrolyte. After TPA separation, succinate can be recycled through the recrystallization process from the remaining electrolyte. The as-collected white TPA and succinate powders are confirmed by XRD patterns. Further details are provided in the Experimental section of the Supporting Information. The electrocatalytic reforming of the 1,4-butanediol component in PBT waste into value-added succinate is sustainable and economic, which improves the profitability of PBT reclaim and highlights the feasibility for practical applications.

To further investigate the BOR behavior on the T-NF, the in-situ Raman spectroscopy was conducted to monitor the surface evolution during the OER and BOR at different potentials. For the OER process, no obvious signals could be detected when the applied potential is below 1.32 V, as shown in Fig. 4a. By increasing the applied potential to 1.35 V, two Raman peaks appear at 476 and 555 cm^{-1} , which are attributed to Ni-O vibrations of NiOOH involved in the OER [41,42]. Their intensities are gradually increased with further increasing the applied potentials. For comparison, after adding BDO, the signals of Ni-O vibrations do not show up until the applied potential reaches 1.70 V (Fig. 4b). It indicates that the oxidation of BDO is accompanied with the reduction of Ni^{3+} in NiOOH, and therefore the appearance of NiOOH is retarded. The in-situ Raman results indicate that NiOOH acts as chemical oxidants toward BDO oxidation and can recycle back to the low-valence Ni species after the reaction. It accounts for the earlier catalytic onset as compared to the OER triggered by the higher-valence Ni^{4+} species.

In Fig. 4c, the evolution of the peaks for NiOOH is further investigated by holding the potential at 1.52 V (vs. RHE). With added 1,4-butanediol in 1.0 M KOH, the two Raman peaks at 476 and 555 cm^{-1} are gradually weakened and then completely disappear after 20 s. It indicates that the reaction between NiOOH and 1,4-butanediol is involved



Scheme 1. Schematic illustration of the process of PBT electro-reforming and product separation; inset: XRD patterns and photographs of self-prepared TPA and succinate.

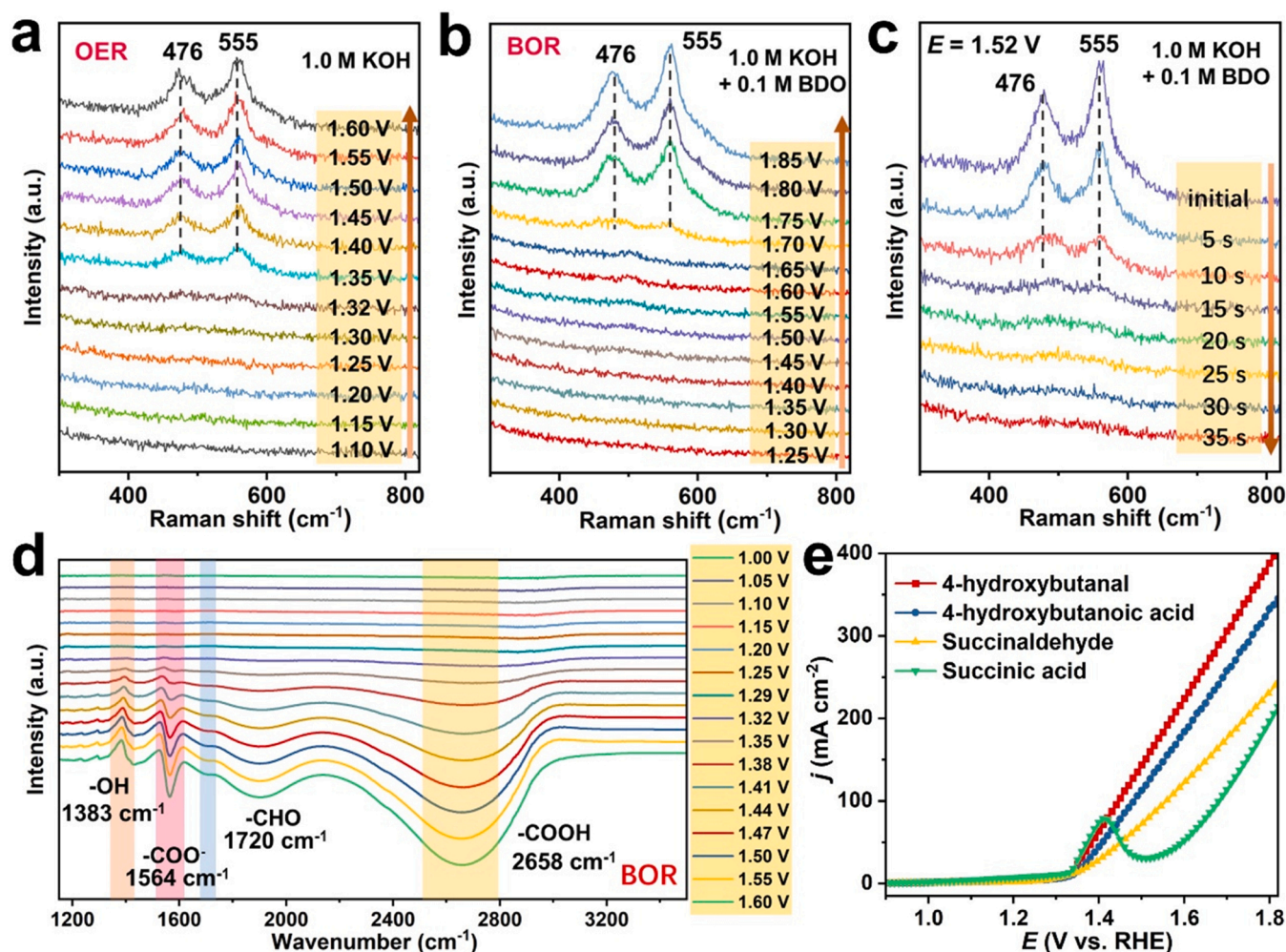


Fig. 4. In-situ Raman spectra of the T-NF during (a) OER (1.0 M KOH) and (b) BOR (1.0 M KOH with 0.1 M BDO) at increased potentials. (c) In-situ Raman spectra of the T-NF at 1.52 V in 1.0 M KOH after the addition of BDO. (d) In-situ FTIR spectra of the T-NF at different applied potentials for the BOR. (e) LSV curves of the T-NF in 1.0 M KOH with adding various possible intermediates.

in the BOR process, with NiOOH as the active species for the 1,4-butanediol oxidation.

To further understand the reaction mechanism and identify the critical reaction intermediates during the BOR process, in-situ FTIR spectra were collected on the T-NF at varied potentials. As shown in Fig. 4d, the absorption bands appear at 1564 cm^{-1} and 2658 cm^{-1} when the potential is increased up to 1.32 V, attributed to the asymmetric O-C-O stretching of COO⁻ and the O-H stretching vibration of COOH, respectively [43,44]. With increasing the potential, the two characteristic peaks become stronger, indicating the generation of succinic acid. The peak at 1720 cm^{-1} can be assigned to the formation of aldehyde intermediates containing carbonyl groups, such as 4-hydroxybutanal and succinaldehyde. Additionally, the reverse absorption peak positioned at 1383 cm^{-1} can be attributed to -OH of 1,4-butanediol. The consumption of 1,4-butanediol results in the enhancement of the reverse absorption peak.

Furthermore, we examined the electrochemical oxidation of possible intermediates of the BOR (4-hydroxybutanal, succinaldehyde, 4-hydroxybutanoic acid, and succinic acid) in 1.0 M KOH solution. As shown in Fig. 4e, the catalytic onsets of 4-hydroxybutanal and 4-hydroxybutanoic acid oxidation occur at similar or lower potentials compared with BDO oxidation, while the succinaldehyde oxidation takes place at slightly higher potentials. By the addition of succinic acid, the oxidation current is not increased in the LSV curve, indicating that the electrochemical oxidation of BDO eventually stops at the reaction stage of succinic acid.

3.4. Theoretical studies

According to the in-situ FTIR and NMR results, aldehyde intermediates exist during the BOR process and they occupy the bifurcation point for further oxidation. Here, a possible pathway for BDO oxidation at the T-NF in an alkaline solution is proposed in Fig. 5a. The BDO oxidation proceeds through the formation of 4-hydroxybutanal followed by two possible oxidation pathways: Pathway I is that the aldehyde group is first oxidized to produce intermediate 4-hydroxybutanoic acid, and then the alcohol group is oxidized to generate the final product succinic acid. Pathway II proceeds through the oxidation of the alcohol group to form succinaldehyde, which then undergoes the oxidation of the aldehyde groups to produce succinic acid.

Density functional theory (DFT) calculations were carried out to reveal the favorable reaction pathway of BDO oxidation on the T-NF. To make the theoretical simulation closer to the real catalyst surface, optimized hybrid NiOOH models and those with main intermediates coordinated were employed to investigate the energetically favorable pathway for BDO oxidation (Figs. 5b and S15-S17). The Gibbs free energy diagrams (ΔG) for BDO oxidation on the T-NF surface with NiOOH active sites are shown in Fig. 5c, and the step with the largest ΔG value represents the rate-determining step (RDS). DFT calculation analyses demonstrate that the O-H bond cleavage of 1,4-butanediol to form OH(CH₂)₃HCO* is an endothermic process with a high ΔG value of 1.45 eV. This value indicates that the formation of OH(CH₂)₃-

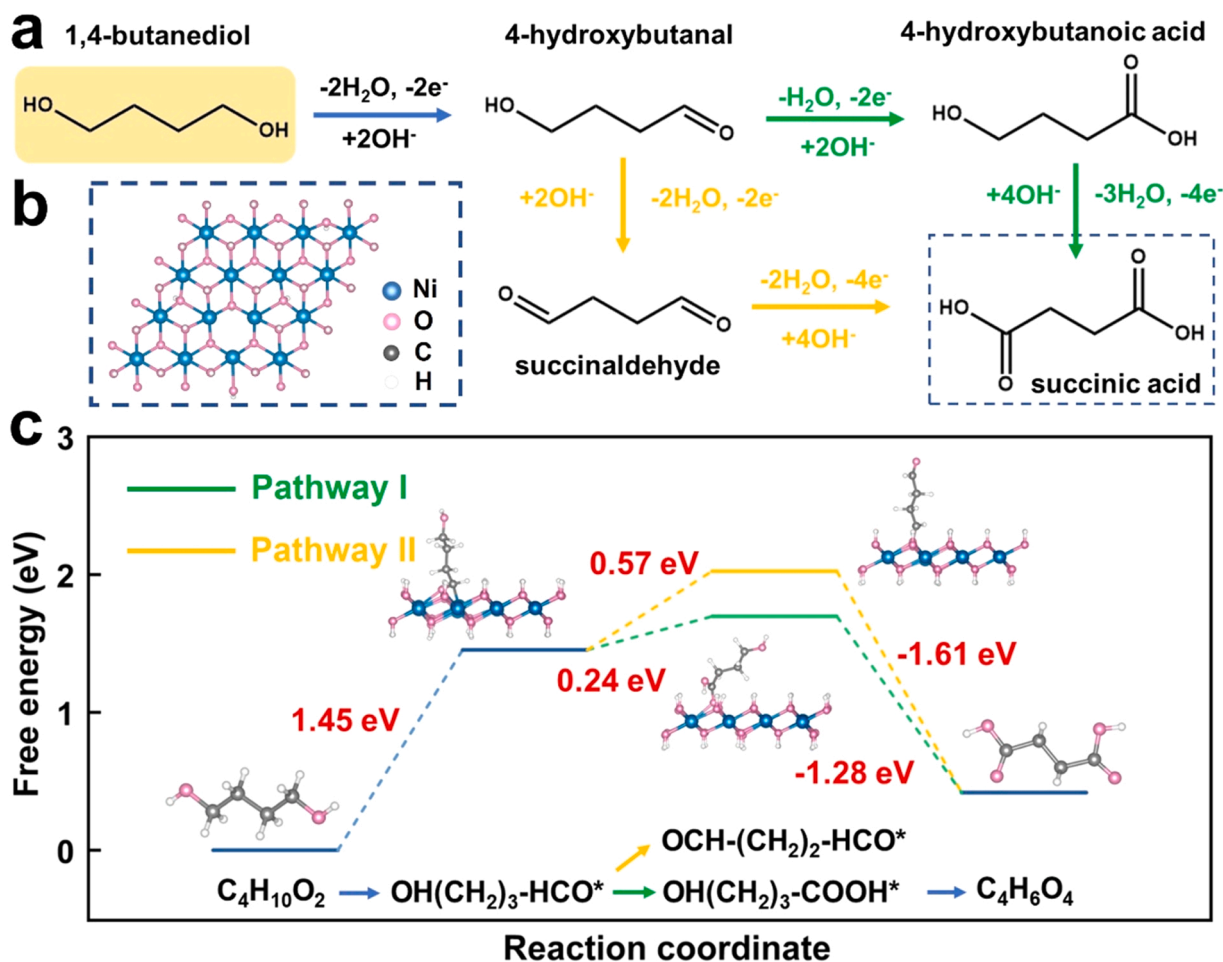


Fig. 5. (a) Proposed reaction pathway of BDO oxidation in alkaline media. (b) Theoretical models for NiOOH active sites. (c) Gibbs free energy diagrams for BDO oxidation to succinic acid.

HCO* intermediate is the RDS for BDO oxidation. This process is associated with a deprotonation step to produce reactive alcohol salt intermediates followed by electron transfer to the electrode [45]. The subsequent cleavage of the O-H or C-H bonds to generate the OH(CH₂)₃-COOH* ($\Delta G = 0.24$ eV) or OCH-(CH₂)₂-HCO* ($\Delta G = 0.57$ eV) intermediate is also an endothermic process. The comparison of the energy barrier values indicates that 1,4-butanediol oxidation on NiOOH tends to form OH(CH₂)₃-COOH* as the second intermediate. This analysis is consistent with the experimental result in Fig. 4e, which reveals the fast oxidation behavior for OH(CH₂)₃-COOH* as compared with OCH-(CH₂)₂-HCO*. Finally, the oxidation of OH(CH₂)₃-COOH* intermediate occurs to generate the final product succinic acid, which is an exothermic process. In this process, the oxidation of alcohol to carboxylates presumably also proceeds through an aldehyde intermediate [46]. Together, the theoretical analysis demonstrates that the oxidation of 1,4-butanediol to succinic acid more likely proceeds through pathway I (BDO \rightarrow OH(CH₂)₃-HCO* \rightarrow OH(CH₂)₃-COOH* \rightarrow succinic acid) and the generation of OH(CH₂)₃-HCO* is identified as the rate-determining step.

3.5. Oxidation of other small organic molecules

To extend the scope of this study, we anticipate that the developed T-NF may potentially work as a multifunctional electrocatalyst. The electrochemical activities toward oxidation of other organic molecules (urea, glycerol, and methanol) were investigated and the polarization curves are presented in Fig. 6a-c. The T-NF electrode delivers a current density of 100 mA cm⁻² at 1.41 V, 1.40 V, and 1.44 V vs. RHE for the

oxidation of urea, glycerol, and methanol, respectively. It also shows small Tafel slopes toward the oxidation of these molecules. The performances are superior to other reported non-noble-metal-based catalysts (Fig. 6d), suggesting the effectiveness and wide applicability of the T-NF electrode.

4. Conclusions

In summary, we developed an ultrafast (6 CV cycles, around 3 min) and versatile NaCl-assisting electro-corrosion approach to transform Ni foams into high-performance, self-supporting catalysts for oxidizing 1,4-butanediol and upcycling PBT waste into value-added chemicals. Studies on corrosion behaviors reveal the important role of Cl⁻ anions and CV scan pattern in preparing the catalytic electrode. The activity of the T-NF electrode is enhanced by 150 times characterized by the integrated Ni²⁺/Ni³⁺ peak area. It delivers a current density of 50 mA cm⁻² at a low potential of 1.36 V for oxidation of 1,4-butanediol to succinate with a high Faraday efficiency of 93%. Similar results are obtained for electrocatalytic reforming of PBT hydrolysate containing 1,4-butanediol monomer. The in-situ Raman and FTIR results reveal NiOOH as the active centers and the key intermediates for the BOR, while DFT calculations identify the favorable pathway for producing succinic acid during the BOR. This work opens up new avenues for the ultrafast activation of the widely used Ni foam and demonstrates its application for upcycling PBT plastic to value-added chemicals.

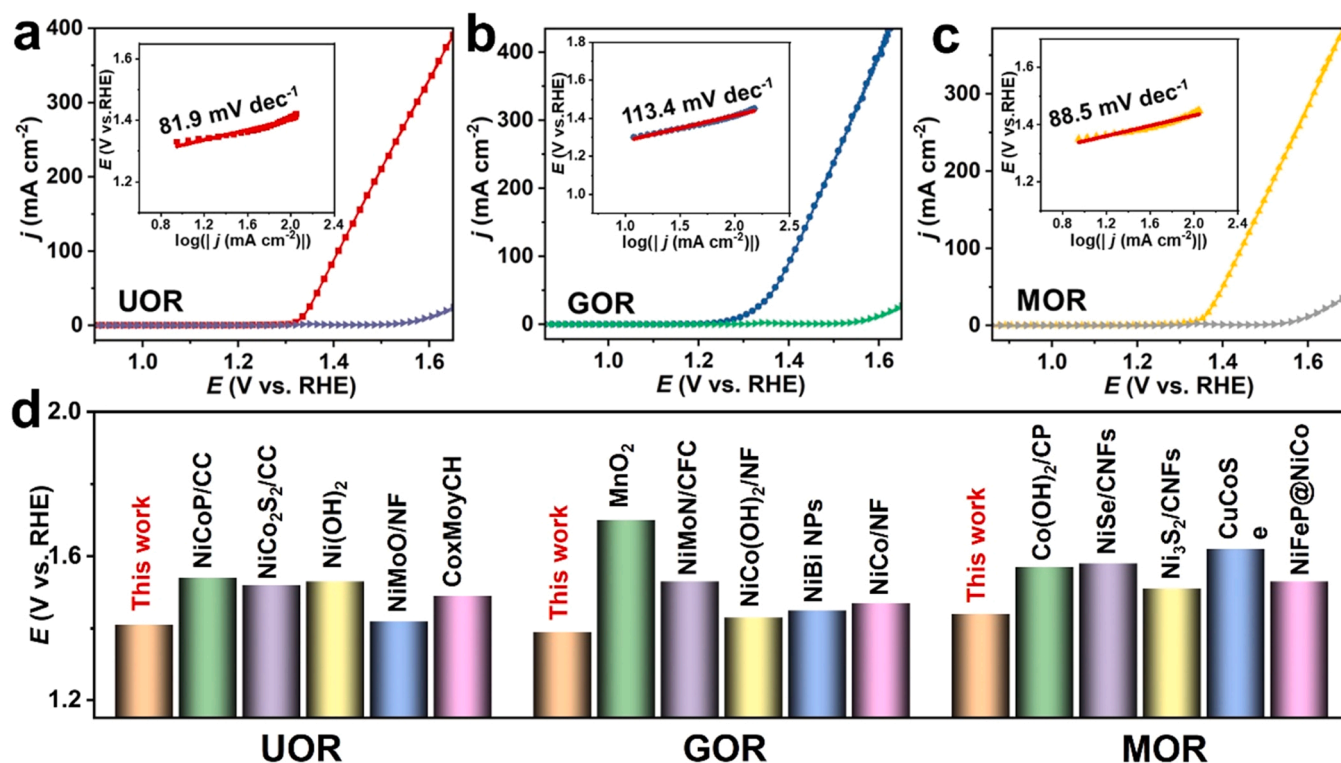


Fig. 6. LSVs and Tafel plots (inset) for the T-NF in 1.0 M KOH with 0.1 M (a) urea, (b) glycerol, and (c) methanol. (d) Comparison of the T-NF over literature reported electrocatalysts for oxidation of urea, glycerol, and methanol (see more details in Table S1).

CRediT authorship contribution statement

X. Liu designed this study, conducted the experiments and wrote the paper; J. Wang, Z. Fang, S. Gong, D. Xiong, W. Chen, D. Wu did some characterizations and performed some data analyses; Z. Chen designed this study, performed some data analyses and revised the paper. All authors contributed to the general discussion.

Declaration of Competing Interest

The authors declare that they have no known competing financial interests or personal relationships that could have appeared to influence the work reported in this paper.

Data availability

Data will be made available on request.

Acknowledgments

This work was supported by the National Natural Science Foundation of China (22072107, 21872105), the Science & Technology Commission of Shanghai Municipality (19DZ2271500), and the Fundamental Research Funds for the Central Universities.

Appendix A. Supplementary material

Supplementary data associated with this article can be found in the online version at [doi:10.1016/j.apcatb.2023.122870](https://doi.org/10.1016/j.apcatb.2023.122870).

References

- [1] L. Li, P. Wang, Q. Shao, X. Huang, Metallic nanostructures with low dimensionality for electrochemical water splitting, *Chem. Soc. Rev.* 49 (2020) 3072–3106.
- [2] Y.-C. Zhang, C. Han, J. Gao, L. Pan, J. Wu, X.-D. Zhu, J.-J. Zou, NiCo-based electrocatalysts for the alkaline oxygen evolution reaction: a review, *ACS Catal.* 11 (2021) 12485–12509.
- [3] X. Liu, Z. Fang, X. Teng, Y. Niu, S. Gong, W. Chen, T.J. Meyer, Z. Chen, Paired formate and H₂ productions via efficient bifunctional Ni-Mo nitride nanowire electrocatalysts, *J. Energy Chem.* 72 (2022) 432–441.
- [4] Y. Niu, X. Teng, S. Gong, M. Xu, S.G. Sun, Z. Chen, Engineering two-phase bifunctional oxygen electrocatalysts with tunable and synergetic components for flexible Zn-air batteries, *Nano-Micro Lett.* 13 (2021) 126.
- [5] W. Luo, Y. Wang, L. Luo, S. Gong, M. Wei, Y. Li, X. Gan, Y. Zhao, Z. Zhu, Z. Li, Single-atom and bimetallic nanoalloy supported on nanotubes as a bifunctional electrocatalyst for ultrahigh-current-density overall water splitting, *ACS Catal.* 12 (2022) 1167–1179.
- [6] X. Mu, X. Gu, S. Dai, J. Chen, Y. Cui, Q. Chen, M. Yu, C. Chen, S. Liu, S. Mu, Breaking the symmetry of single-atom catalysts enables an extremely low energy barrier and high stability for large-current-density water splitting, *Energy Environ. Sci.* 15 (2022) 4048–4057.
- [7] H. Liu, R. Xie, Y. Luo, Z. Cui, Q. Yu, Z. Gao, Z. Zhang, F. Yang, X. Kang, S. Ge, S. Li, X. Gao, G. Chai, L. Liu, B. Liu, Dual interfacial engineering of a Chevrel phase electrode material for stable hydrogen evolution at 2500 mA cm⁻², *Nat. Commun.* 13 (2022) 6382.
- [8] T. Xu, D. Jiao, M. Liu, L. Zhang, X. Fan, L. Zheng, W. Zheng, X. Cui, Ni center coordination reconstructed nanocorals for efficient water splitting, *Adv. Sci.* (2022) 2205605.
- [9] C. Deng, C.Y. Toe, X. Li, J. Tan, H. Yang, Q. Hu, C. He, Earth-abundant metal-based electrocatalysts promoted anodic reaction in hybrid water electrolysis for efficient hydrogen production: recent progress and perspectives, *Adv. Energy Mater.* 12 (2022) 2201047.
- [10] X. Fu, R. Shi, S. Jiao, M. Li, Q. Li, Structural design for electrocatalytic water splitting to realize industrial-scale deployment: strategies, advances, and perspectives, *J. Energy Chem.* 70 (2022) 129–153.
- [11] G. Qian, J. Chen, T. Yu, J. Liu, L. Luo, S. Yin, Three-phase heterojunction nimo-based nano-needle for water splitting at industrial alkaline condition, *Nano-Micro Lett.* 14 (2021) 20.
- [12] J. Zhu, L. Hu, P. Zhao, L.Y.S. Lee, K.Y. Wong, Recent advances in electrocatalytic hydrogen evolution using nanoparticles, *Chem. Rev.* 120 (2020) 851–918.
- [13] X. Liu, M. Gong, S. Deng, T. Zhao, T. Shen, J. Zhang, D. Wang, Transforming damage into benefit: corrosion engineering enabled electrocatalysts for water splitting, *Adv. Funct. Mater.* 31 (2020) 2009032.
- [14] S. Hao, L. Chen, C. Yu, B. Yang, Z. Li, Y. Hou, L. Lei, X. Zhang, NiCoMo hydroxide nanosheet arrays synthesized via chloride corrosion for overall water splitting, *ACS Energy Lett.* 4 (2019) 952–959.
- [15] L. Yu, L. Wu, B. McElhenny, S. Song, D. Luo, F. Zhang, Y. Yu, S. Chen, Z. Ren, Ultrafast room-temperature synthesis of porous S-doped Ni/Fe (oxy)hydroxide

- electrodes for oxygen evolution catalysis in seawater splitting, *Energy Environ. Sci.* 13 (2020) 3439–3446.
- [16] B. Fei, Z. Chen, J. Liu, H. Xu, X. Yan, H. Qing, M. Chen, R. Wu, Ultrathinning nickel sulfide with modulated electron density for efficient water splitting, *Adv. Energy Mater.* 10 (2020) 2001963.
- [17] L. Gong, H. Yang, H. Wang, R. Qi, J. Wang, S. Chen, B. You, Z. Dong, H. Liu, B. Y. Xia, Corrosion formation and phase transformation of nickel-iron hydroxide nanosheets array for efficient water oxidation, *Nano Res.* 14 (2021) 4528–4533.
- [18] T. Jiang, K. Li, S. Park, K. Zheng, Y. Meng, Y. Yuan, Z. Liu, Z. Zhu, X. Zheng, S. Liu, W. Chen, Facile fabrication of bifunctional hydrogen catalytic electrodes for long-life nickel-hydrogen gas batteries, *Nano Lett.* 22 (2022) 1741–1749.
- [19] X. Liu, M. Gong, D. Xiao, S. Deng, J. Liang, T. Zhao, Y. Lu, T. Shen, J. Zhang, D. Wang, Turning waste into treasure: regulating the oxygen corrosion on Fe foam for efficient electrocatalysis, *Small* 16 (2020) 2000663.
- [20] W. Zhao, H. Xu, H. Luan, N. Chen, P. Gong, K. Yao, Y. Shen, Y. Shao, NiFe layered double hydroxides grown on a corrosion-cell cathode for oxygen evolution electrocatalysis, *Adv. Energy Mater.* 12 (2021) 2102372.
- [21] Y. Li, X. Wei, L. Chen, J. Shi, Electrocatalytic hydrogen production trilogy, *Angew. Chem. Int. Ed.* 60 (2021) 19550–19571.
- [22] H.Y. Wang, M.L. Sun, J.T. Ren, Z.Y. Yuan, Circumventing challenges: design of anodic electrocatalysts for hybrid water electrolysis systems, *Adv. Energy Mater.* 13 (2022) 2203568.
- [23] T. Wang, X. Cao, L. Jiao, Progress in hydrogen production coupled with electrochemical oxidation of small molecules, *Angew. Chem. Int. Ed.* 61 (2022), 20223328.
- [24] M.-Q. Zhang, M. Wang, B. Sun, C. Hu, D. Xiao, D. Ma, Catalytic strategies for upvaluing plastic wastes, *Chem* 8 (2022) 2912–2923.
- [25] Z. Gao, B. Ma, S. Chen, J. Tian, C. Zhao, Converting waste PET plastics into automobile fuels and antifreeze components, *Nat. Commun.* 13 (2022) 3343.
- [26] Y. Kratish, T.J. Marks, Efficient polyester hydrogenolytic deconstruction via tandem catalysis, *Angew. Chem. Int. Ed.* 61 (2022) 202112576.
- [27] N. Nghiem, S. Kleff, S. Schwegmann, Succinic acid: technology development and commercialization, *Fermentation* 3 (2017) 223–239.
- [28] D. Silva, E. Bogel-Lukasik, Valuable new platform chemicals obtained by valorisation of a model succinic acid and bio-succinic acid with an ionic liquid and high-pressure carbon dioxide, *Green Chem.* 19 (2017) 4048–4060.
- [29] Q. Yu, Z. Cui, Y. Zheng, H. Huo, L. Meng, J. Xu, C. Gao, Exploring succinic acid production by engineered *Yarrowia lipolytica* strains using glucose at low pH, *Biochem. Eng. J.* 139 (2018) 51–56.
- [30] X. Liu, Z. Fang, D. Xiong, S. Gong, Y. Niu, W. Chen, Z. Chen, Upcycling PET in parallel with energy-saving H₂ production via bifunctional nickel-cobalt nitride nanosheets, *Nano Res.* (2022), <https://doi.org/10.1007/s12274-022-5085-9>.
- [31] J. Wang, X. Li, M. Wang, T. Zhang, X. Chai, J. Lu, T. Wang, Y. Zhao, D. Ma, Electrocatalytic valorization of poly(ethylene terephthalate) plastic and CO₂ for simultaneous production of formic acid, *ACS Catal.* 12 (2022) 6722–6728.
- [32] J. Wang, X. Li, T. Zhang, Y. Chen, T. Wang, Y. Zhao, Electro-reforming polyethylene terephthalate plastic to co-produce valued chemicals and green hydrogen, *J. Phys. Chem. Lett.* 13 (2022) 622–627.
- [33] F. Liu, X. Gao, R. Shi, Z. Guo, E.C.M. Tse, Y. Chen, Concerted and selective electrooxidation of polyethylene-terephthalate-derived alcohol to glycolic acid at an industry-level current density over a Pd-Ni(OH)₂ catalyst, *Angew. Chem. Int. Ed.* 62 (2023), e202300094.
- [34] R. Shi, K.S. Liu, F. Liu, X. Yang, C.C. Hou, Y. Chen, Electrocatalytic reforming of waste plastics into high value-added chemicals and hydrogen fuel, *Chem. Commun.* 57 (2021) 12595–12598.
- [35] Y. Yan, H. Zhou, S.M. Xu, J. Yang, P. Hao, X. Cai, Y. Ren, M. Xu, X. Kong, M. Shao, Z. Li, H. Duan, Electrocatalytic upcycling of biomass and plastic wastes to biodegradable polymer monomers and hydrogen fuel at high current densities, *J. Am. Chem. Soc.* 145 (2023) 6144–6155.
- [36] H. Zhou, Y. Ren, Z. Li, M. Xu, Y. Wang, R. Ge, X. Kong, L. Zheng, H. Duan, Electrocatalytic upcycling of polyethylene terephthalate to commodity chemicals and H₂ fuel, *Nat. Commun.* 12 (2021) 4679.
- [37] J. Hao, J. Liu, D. Wu, M. Chen, Y. Liang, Q. Wang, L. Wang, X.-Z. Fu, J.-L. Luo, In situ facile fabrication of Ni(OH)₂ nanosheet arrays for electrocatalytic co-production of formate and hydrogen from methanol in alkaline solution, *Appl. Catal. B Environ.* 281 (2021), 119510.
- [38] F. Ma, S. Wang, X. Gong, X. Liu, Z. Wang, P. Wang, Y. Liu, H. Cheng, Y. Dai, Z. Zheng, B. Huang, Highly efficient electrocatalytic hydrogen evolution coupled with upcycling of microplastics in seawater enabled via Ni₃N/W₅N₄ janus nanostructures, *Appl. Catal. B Environ.* 307 (2022), 121198.
- [39] X. Qiao, X. Yin, L. Wen, X. Chen, J. Li, H. Ye, X. Huang, W. Zhao, T. Wang, Variable nanosheets for highly efficient oxygen evolution reaction, *Chem* 8 (2022) 3241–3251.
- [40] F. Yang, Y. Luo, Q. Yu, Z. Zhang, S. Zhang, Z. Liu, W. Ren, H.M. Cheng, J. Li, B. Liu, A durable and efficient electrocatalyst for saline water splitting with current density exceeding 2000 mA cm⁻², *Adv. Funct. Mater.* 31 (2021) 2010367.
- [41] Y. Huang, X. Chong, C. Liu, Y. Liang, B. Zhang, Boosting hydrogen production by anodic oxidation of primary amines over a NiSe nanorod electrode, *Angew. Chem. Int. Ed.* 57 (2018) 13163–13166.
- [42] B. Zhao, J. Liu, X. Wang, C. Xu, P. Sui, R. Feng, L. Wang, J. Zhang, J.-L. Luo, X.-Z. Fu, CO₂-emission-free electrocatalytic CH₃OH selective upgrading with high productivity at large current densities for energy saved hydrogen co-generation, *Nano Energy* 80 (2021), 105530.
- [43] Y. Li, X. Wei, S. Han, L. Chen, J. Shi, MnO₂ electrocatalysts coordinating alcohol oxidation for ultra-durable hydrogen and chemical productions in acidic solutions, *Angew. Chem. Int. Ed.* 60 (2021) 21464–21472.
- [44] C.C. Lima, M.V.F. Rodrigues, A.F.M. Neto, C.R. Zanata, C.T.G.V.M.T. Pires, L. S. Costa, J. Solla-Gullón, P.S. Fernández, Highly active Ag/C nanoparticles containing ultra-low quantities of sub-surface Pt for the electrooxidation of glycerol in alkaline media, *Appl. Catal. B Environ.* 279 (2020), 119369.
- [45] Y. Kwon, S.C. Lai, P. Rodriguez, M.T. Koper, Electrocatalytic oxidation of alcohols on gold in alkaline media: base or gold catalysis? *J. Am. Chem. Soc.* 133 (2011) 6914–6917.
- [46] J. Wu, J. Li, Y. Li, X.Y. Ma, W.Y. Zhang, Y. Hao, W.B. Cai, Z.P. Liu, M. Gong, Steering the glycerol electro-reforming selectivity via cation-intermediate interactions, *Angew. Chem. Int. Ed.* 61 (2022) 202113362.